$1g_{9/2}$, $1f_{5/2}$, and $1f_{7/2}$ neutron inner hole responses in ^{115}Sn and ^{119}Sn via the $(\vec{d},t)$ reaction at $E_d=200$ MeV

H. Langevin-Joliot,[1] J. Van de Wiele,[1] J. Guillot,[1] E. Gerlic,[2] L. H. Rosier,[1] A. Willis,[1] C. Djalali,[1,3] M. Morlet,[1] E. Tomasi-Gustafsson,[4] N. Blasi,[5] S. Micheletti,[5] and S. Y. van der Werf[6]

[1]*Institut de Physique Nucléaire, IN2P3-CNRS, Boîte Postale N°1-91406 Orsay, France*

[2]*Institut de Physique Nucléaire, IN2P3-CNRS, 43 Bd du 11 Novembre, 69622 Lyon-Villeurbanne, France*

[3]*Department of Physics and Astronomy, University of South Carolina, Columbia, South Carolina 29208*

[4]*DAPNIA-SPhN and Laboratoire National Saturne, CEN-Saclay, F 91191, Gif sur Yvette, France*

[5]*INFN and University of Milan, Physics Department, Via Celoria 16, 20133 Milan, Italy*

[6]*Kernfysisch Versneller Instituut, 9747 AA Groningen, The Netherlands*

(Received 17 May 2002; published 11 November 2002)

Neutron inner hole responses in ^{115}Sn and ^{119}Sn nuclei have been studied via the $(\vec{d},t)$ reaction at $E_d=200$ MeV using a polarized beam with both vector and tensor components. One-step pickup observables corresponding to the overlapping $1g_{9/2}$, $1f_{5/2}$, and $1f_{7/2}$ responses were analyzed between 3° and 15° via a least square fit procedure up to $E_X=21.5$ MeV and 20 MeV in ^{115}Sn and ^{119}Sn, respectively. The relative enhancement of transitions with high total angular momentum j and the strongly characteristic angular distributions of $j_-=l-1/2$ versus $j_+=l+1/2$ vector and tensor analyzing powers allow the extraction for the first time of $1f_{5/2}$ and $1f_{7/2}$ strength distributions and of new $1g_{9/2}$ strength in addition to its previously known main component. The standard DWBA analysis is complemented by a refined analysis taking into account the form factor dependence on excitation energy due to the hole coupling with surface vibrations calculated in the framework of the quasiparticle-phonon coupling model (QPMFF). Residual nucleus spectra were measured, mainly in ^{115}Sn, up to $E_X\sim45$ MeV where the underlying background of multistep reactions is dominant and can be calibrated. The background of multistep pickup cross section is calculated for the first time in the forward angle region, assuming a dominant role of collective excitations in inelastic steps. Coupled channel calculations for two-step pickup observables involving low multipole collective excitations are performed for comparison. Integrated strengths deduced in the present work are compared with previous data on the $1g_{9/2}$ structure and tail, and with the very limited previous information existing on the $1f$ strengths. The $1g_{9/2}$, $1f_{5/2}$, and $1f_{7/2}$ QPMFF and standard strength distributions are compared with available theoretical predictions. In particular, we find that the $1f_{5/2}$ and $1f_{7/2}$ strength distributions are not well reproduced by the QPM model. The QPMFF spreading widths are found much narrower than the standard ones, but nevertheless much wider than predicted by theoretical calculations.

DOI: 10.1103/PhysRevC.66.054303 PACS number(s): 21.10.Pc, 25.45.Hi, 24.70.+s, 24.10.Eq

I. INTRODUCTION

Neutron inner hole states have been studied in a number of medium weight and heavy nuclei via pickup reactions [1], since the pioneering work of Sakai and Kubo [2]. In particular, inner hole state responses in tin nuclei have been investigated via different pickup reactions such as (p,d) [3–8], (d,t) [9–15] and $(^3\mathrm{He},\alpha)$ [3,16–20]. These experiments have given evidence for a strong concentration of the $1g_{9/2}$ strength, especially in the light tin isotopes, around typically $E_X=5.3$ MeV. The $2p$ strengths have been found partly concentrated in a broad bump around 6 MeV [8,11]. The $1g_{9/2}$ and $2p$ giant-resonance-like structures have been shown to be fragmented in many groups [5,10,12,13,19]. Their gamma or neutron decay has been studied in selected cases [21–23]. The knowledge of the $1g_{9/2}$ and $2p$ strengths beyond the main structures however suffers of severe uncertainties. Moreover, the information gained up to now on the higher lying $1f_{5/2}$ and $1f_{7/2}$ hole states in tin isotopes [3,14,15,20] is very limited and bears only on integrated strengths.

The role of the coupling of quasiparticle degrees of freedom to the surface modes has been a subject of special interest for many years [24–27]. It has been shown that this coupling is responsible for major features of neutron hole strength fragmentation. Microscopic calculations for tin nuclei have focussed mainly on the $1g_{9/2}$ and $2p$ strength distributions [25,28,29]. The quasiparticle-phonon model [24] (hereafter QPM model) has also been used later to calculate the $1f_{5/2}$ and $1f_{7/2}$ strength distributions [30,31].

We performed a new investigation of the overlapping $1g_{9/2}$, $1f_{5/2}$, and $1f_{7/2}$ inner hole states in ^{115}Sn and ^{119}Sn to achieve a quantitative determination of their strength distributions up to excitation energies $E_X=21.5$ MeV and $E_X=20$ MeV, respectively.

Neutron hole states were populated via the $(\vec{d},t)$ reaction using a vector and tensor polarized deuteron beam at 200 MeV incident energy. As shown in our systematic study of valence levels in medium weight and heavy nuclei [32], the reaction at this high incident energy is strongly selective for the population of hole states with large angular momentum l. Both vector and tensor analyzing powers allow a clear identification of $j_+=l+1/2$ versus $j_-=l-1/2$ transitions.

A critical point in the determination of strength distributions resulting from DWBA analyses, neglected in previous

studies of tin nuclei, is the dependence of form factors on the hole coupling with surface vibrations. An investigation of this dependence performed in the framework of the QPM model for several hole states in ^{208}Pb has shown a significant increase of form factor radii with separation energy [33]. This effect proved quite important in our analysis of the ^{208}Pb$(\vec{d},t)^{207}$Pb reaction [34]. It is taken into account in the present work following the same approach. The strength distributions resulting from this improved analysis (hereafter QPMFF strength distributions) are systematically compared with those deduced in a standard analysis assuming no dependence of DWBA observables on excitation energy for transitions of same nlj.

It is also well known that determinations of inner hole response functions are hampered by the contribution of multistep pickup reactions to the experimental spectra. We measured the ^{115}Sn excitation energy spectra up to $E_X = 45$ MeV to achieve this multistep background at the highest excitation energies where it dominates the spectra. We present in this paper a calculation of two-step and multistep pickup cross-section spectra. The multi-step calculation code of Koning and Akkermans [35] was adapted to take into account the expected dominant role of collective excitations in inelastic steps. Two-step pickup cross-section spectra were independently obtained via coupled channel calculations with the method described in Ref. [34]. Analyzing powers are calculated in addition to cross sections with this latter method.

The paper is organized as follows. The experimental procedure and the raw data are presented in Sec. II. The data reduction, the one-step pickup analysis and the multistep background calculations are described in Sec. III. Experimental results are presented in Sec. IV and compared with previous data and theoretical predictions of strength distributions. Section V summarizes the conclusions.

II. EXPERIMENTAL PROCEDURE AND OVERALL FEATURES OF THE DATA

The experiment was performed with the 200 MeV polarized deuteron beam available at the laboratoire national saturne (LNS). Deuterons, polarized in four different states [36] which are linear combinations of vector and tensor polarization states, were accelerated sequentially every four successive bursts. The vector and tensor polarization parameters ρ_{10} and ρ_{20} of the deuteron beam were periodically measured with the low energy $d(\vec{d},p)t$ polarimeter [36]. They were found stable at $\rho_{10} = -0.375 \pm 0.008$ and $\rho_{20} = 0.64 \pm 0.006$, which correspond to 92% and 90.5% of their maximum values, respectively.

The $(\vec{d},t)$ reaction was studied on a ^{116}Sn target (97.5% enriched) and a ^{120}Sn target (99.6% enriched) of 39.9 mg cm^{-2} and 39.6 mg cm^{-2} thickness, respectively. The experimental setup has been described in Ref. [32].

The outgoing particles labeled with the corresponding deuteron polarized state were analyzed by the high resolution spectrometer SPES1 working in the dispersion matching mode. The first three localization chambers of the polarimeter ''POMME'' [37] were used to measure the trajectory positions and angles at the focal plane. The numbers of events measured at each focal plane position for the different polarized states were combined according to the formula given in Ref. [32] to get cross-section excitation energy spectra $\sigma(E_x)$ and analyzing power dependent spectra $\sigma(E_x)\cdot A_y(E_x)$ and $\sigma(E_x)\cdot A_{yy}(E_x)$. The POMME detection system and the rather thick exit window of the spectrometer contribute together 80–100 keV to the 200 keV total energy resolution. The horizontal and vertical angular acceptances were set, respectively, at 2° and 4°, partly achieved with software cuttings. Energy loss and time of flight of the detected particles were continuously measured in the ''POMME'' trigger. The data were taken in 3° steps from 3° to 15°, the use of several settings of the spectrometer magnetic field allowing the study of ^{115}Sn and ^{119}Sn up to $E_X = 45$ MeV and 21 MeV, respectively, at all angles. An additional measurement was performed for ^{119}Sn at 15° with the magnetic setting centered at $E_X = 43$ MeV.

The spectrometer's high dispersion and good optical qualities allowed already an excellent selection of high energy tritons which have much larger magnetic rigidities than other particles. Trajectory reconstruction from the focal plane to the target was used to suppress a small number of tritons produced in the target frame by the beam halo. The ratio of empty frame to target-in tritons was always $\leqslant 1\%$ under these conditions. No subtraction of the widely spread empty frame tritons was performed. The reaction triton spectra were corrected for the 1–3 % losses resulting from the geometrical cuttings.

Deuteron contribution at the focal plane was found completely negligible at most angles and magnetic field settings. A 15% spurious contribution of deuterons scattered by the thick target and rescattered and slowed down in the spectrometer chamber box was observed at 3° with the magnetic setting set for the measurement of tin excitation energy spectra above ~ 35 MeV. In this latter case, the characteristic triton peak raised in time of flight and energy loss spectra over a pedestal produced by the slowed down deuterons. Excitation energy spectra obtained by selecting off line deuterons on both side of the triton peak were used to approximate and subtract out the contribution to the triton spectra of the deuteron appearing under the peak and selected with it. Estimated error on this procedure is $\sim 3\%$.

Two scintillator telescopes, one in the reaction plane at $-45°$, the other in the vertical plane at 50° were used to continuously monitor the beam current. The integrated counts of each telescope were averaged over the four polarization states. The two beam monitors were calibrated for each target by the carbon activation method used at the LNS [38]. Systematic errors in the calibration are less than 15%. The cross sections calculated using the two beam monitors agreed within less than 10% (generally 5%) and statistical errors were generally very small. We adopted conservatively an uncertainty of 10% on cross sections at each angle (or the statistical errors if larger). Calibration of the low energy polarimeter with dead time corrections may account for 5% systematic error on the measured analyzing powers.

Typical excitation energy spectra are presented in Figs. 1

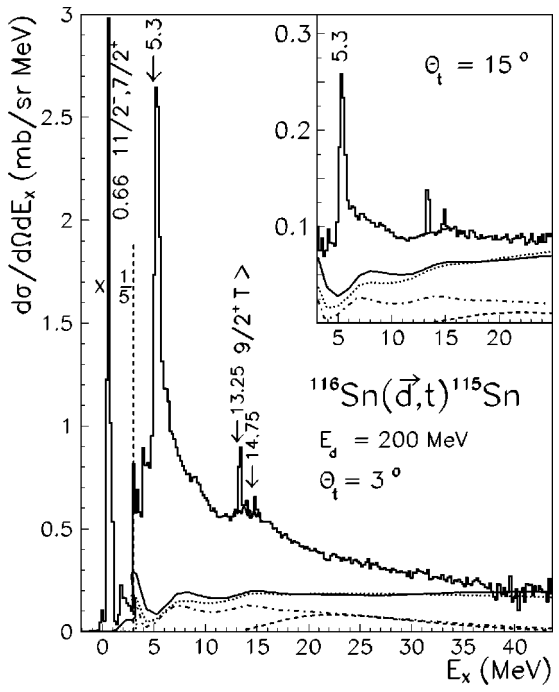

FIG. 1. Excitation energy spectra of the residual nucleus ^{115}Sn compressed in 200 keV energy bins. The solid, dotted, and dash-dotted lines are calculated background spectra referred to as back1 and back2, and two-step cross-sections spectra involving $L=1-3$ excitations, respectively (see Sec. III B). The dashed line is the deep shells contribution.

and 2 for ^{115}Sn and ^{119}Sn, respectively. The main contributions of the valence levels in the ^{115}Sn spectra merge into the peak below 1 MeV, while many unresolved valence levels with small spectroscopic factors and large collective components contribute to the intermediate energy region upto $E_X \sim 3.7$ MeV [19]. Above this energy, the spectra are dominated by the well known $1g_{9/2}$ peak. Moreover, they exhibit a bump around $E_X = 14.5$ MeV, which is significantly more pronounced than observed in previous experiments. Beyond the bump, the spectra decrease smoothly towards the highest

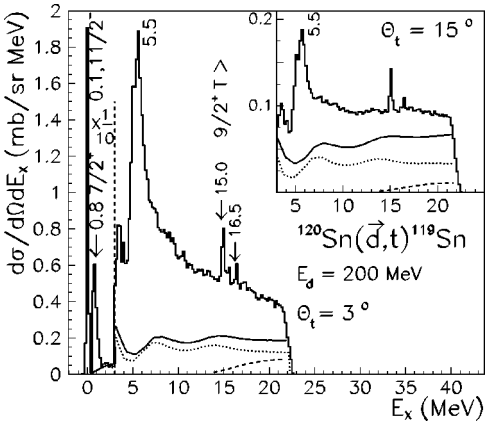

FIG. 2. Excitation energy spectra of the residual nucleus ^{119}Sn compressed in 200 keV energy bins. Solid and dashed lines as in Fig. 1. Dotted line: Total two-step pickup contribution to the background back1.

excitation energy. A much more pronounced slope would be expected for a pure direct pickup spectrum, as the contributing l transfers and nucleon numbers decrease from one major shell to the next deeper one. This points to important contributions of multistep processes, as discussed later on. The $1h_{11/2}$ and $1g_{7/2}$ first valence levels, well separated in ^{119}Sn, give direct evidence for the reaction selectivity for the largest l transfers. The ^{119}Sn spectra are rather similar to the ^{115}Sn ones beyond the valence region, as expected. The $1g_{9/2}$ quasihole peak is, however, less pronounced, in agreement with previous works, and no clear indication for a bump at higher excitation energy is found. Contributions of the narrow isobaric analog peaks rising over the two tin spectra were subtracted out.

III. DATA REDUCTION AND DETERMINATION OF SPECTROSCOPIC STRENGTHS

The valence level results on ^{115}Sn and ^{119}Sn have been published previously in our survey of the $(\vec{d},t)$ reaction at 200 MeV [32] on nuclei from ^{12}C to ^{208}Pb. We summarize in the following several conclusions of this survey which are important for the present work.

The reaction allows a very clear identification of $j_- = l - 1/2$ versus $j_+ = l + 1/2$ states with quantum number $n=1$. This identification relies on both vector and tensor analyzing power angular distributions, as shown in Fig. 3 in the case of the $1h_{11/2}$ and $1g_{7/2}$ first valence levels in ^{119}Sn. The $2d_{5/2}$ level angular distributions are also shown for comparison. The experimental angular distributions are successfully described by finite range distorted wave calculations (DWBA) using S and D range functions deduced from the super soft core interaction and optical parameters given in Ref. [32]. Such DWBA calculations predict very similar angular distribution shapes for hole state of the same type (j_- or j_+) belonging to different shells or nuclei. Experimental angular distributions measured in different nuclei support this conclusion. The reaction is strongly selective for the population of hole states with high l orbital momentum, especially of j_+ type. For example, $1g_{9/2}$, $1f_{5/2}$, $1f_{7/2}$ and $2p$ cross sections in tin nuclei averaged over the angular range of the present experiment would be typically in the ratio 1/0.22/0.37/0.14 for equal spectroscopic strengths.

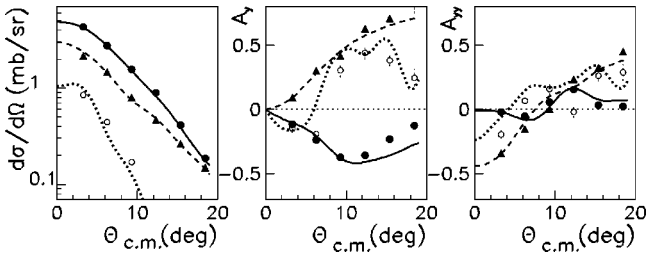

FIG. 3. Angular distributions of the $1h_{11/2}$ (filled circles), $1g_{7/2}$ (triangles), and $2d_{5/2}$ (open circles) levels at 0.09 MeV, 0.79 MeV, and 1.09 MeV, respectively, in ^{119}Sn with corresponding DWBA curves (from Ref. [33]).

A. Data reduction, DWBA analyses and fitting procedure

The experimental spectra between $E_X = 3.7$ MeV and $E_X = 21.5$ MeV in ^{115}Sn (20 MeV in ^{119}Sn) were divided into excitation energy bins. The bin widths were increased from ~ 0.5 MeV in the $1g_{9/2}$ structure region up to 2.5 MeV for the high excitation energy bins to improve the statistic on analyzing power determination. Many collective levels with small valence strength contribute to the spectra below $E_X = 3.7$ MeV while the multistep pickup background dominates beyond $E_X \sim 20$ MeV.

The determination of hole strength distributions relies on DWBA analyses of one-step pickup spectra. Multistep pickup constitutes a physical background which must be subtracted out of the experimental data. The methods used to calculate the background are presented later on in Sec. III B. Its contribution around 20 MeV excitation energy accounts for $\sim 45\%$ and $\sim 75\%$ in both tin data at 3° and 15°, respectively, as shown in Fig. 1 and Fig. 2. One-step pickup populating hole states deeper than $1f_{7/2}$ (hereafter deep shells) is expected to give widely energy spread and rather small cross sections. This deep shells contribution was calculated with the method described in Ref. [34]. DWBA calculations were performed for each of these full subshells at the Hartree-Fock separation energy predicted with the Skyrme III force [39]. Gaussian-type strength distributions [27] with parameters $\Gamma_\infty = 26$ MeV and $A = 550$ were adopted. The corresponding spreading widths range from ~ 11 MeV for the $1d_{3/2}$ deep hole to ~ 19 MeV for the $1s_{1/2}$ hole. As shown in Fig. 1, the deep shells cross-sections around $E_X = 20$ MeV account for $\sim 25\%$ and $\sim 12\%$ of the experimental cross sections, respectively, at 3° and 15°.

Three experimental observables σ^{exp}, $\sigma^{exp}A_y^{exp}$, and $\sigma^{exp}A_{yy}^{exp}$ were obtained at each angle by integrating the data over the excitation energy range of the considered bin. The deep shells observables σ^d, $\sigma^d A_y^d$, and $\sigma^d A_{yy}^d$ and the background observables σ^b, $\sigma^d A_y^b$, and $\sigma^b A_{yy}^d$ were deduced by integrating the corresponding calculated spectra.

One-step pickup observables were obtained by subtracting out deep shells and background contributions, as indicated in Eqs. (1):

$$\sum_i \mathcal{S}_i \sigma_i^{th} = \sigma^{exp} - \sigma^d - \sigma^b,$$

$$\sum_i \mathcal{S}_i \sigma_i^{th} A_{yi}^{th} = \sigma^{exp} A_y^{exp} - \sigma^d A_y^d - \sigma^b A_y^b,$$

$$\sum_i \mathcal{S}_i \sigma_i^{th} A_{yyi}^{th} = \sigma^{exp} A_{yy}^{exp} - \sigma^d A_{yy}^d - \sigma^b A_{yy}^b. \qquad (1)$$

They appear in Eqs. (1) as linear sums of products of DWBA calculated observables σ^{th}, $\sigma^{th}A_y^{th}$, and $\sigma^{th}A_{yy}^{th}$ for subshells i ($1g_{9/2}$, $2p_{1/2,3/2}$, $1f_{5/2}$, $1f_{7/2}$) and of the spectroscopic strengths $\mathcal{S}_i$ to extract in the considered bin. DWBA calculations were performed for each full strength with the code DWUCK5 [40] with the parameters used for valence levels and for separation energies about 2 MeV lower than predicted by Hartree-Fock calculations, as suggested in Ref. [27]. $2p$ DWBA observables were taken as weighed sums of $2p_{1/2}$ and $2p_{3/2}$ transitions.

Typical one-step pickup angular distributions are shown in Fig. 4 for several excitation energy bins in ^{115}Sn. The error bars take into account estimated systematic errors on the subtracted deep shells and background contributions (here cross sections back1 and analyzing powers backa defined in Sec. III B). The two or three dominant spectroscopic strengths residing in each energy bin have been extracted via a least square fit procedure as in Ref. [34]. The strong similarity of $1g_{9/2}$ and $1f_{7/2}$ predicted angular distributions prevents a confident determination of their relative strength in intermediate excitation energy bins where both could contribute. So, either $1g_{9/2}$ or $1f_{7/2}$ was taken into account in the fits. Slightly better χ^2 values were achieved with $1g_{9/2}$ than $1f_{7/2}$ below $E_X \sim 10$ MeV excitation energy and with $1f_{7/2}$ beyond $E_X \sim 12$ MeV. The distribution of the $1g_{9/2}$ strength extracted with no contribution of the $1f_{7/2}$ strength and of $1f_{7/2}$ without $1g_{9/2}$ led us to locate better the two strength overlap between ~ 10 MeV and ~ 15 MeV in ^{115}Sn (0.3 to 1 MeV higher in ^{119}Sn). The $1g_{9/2}$ and $1f_{7/2}$ strengths in the corresponding bins were corrected accordingly.

The $2p$ strength was taken into account in the fitting procedure up to $E_X \sim 15$ MeV. The resulting strengths in the different energy bins are rather poorly determined, as expected for hole states with such a low angular momentum l, the strength integrated over all bins exhausting approximately the sum rule. The fits including the $2p$ strength give generally improved χ^2 values compared to those of hole states with large angular momentum l alone, especially below $E_X \sim 7$ MeV where the $2p$ strength is known to be mostly concentrated [8,11]. The extracted $1f_{5/2}$ is then significantly modified while the other strengths are nearly unchanged.

The calculated angular distributions corresponding to the best fits reproduce well the data, as shown in Fig. 4. Angular distributions fits with two transitions only or with pure transitions are shown for comparison. The systematically negative values of the vector analyzing powers deduced from experiment are easily explained by the dominant cross sections of $1g_{9/2}$ or $1f_{7/2}$ transitions. Negative values of tensor analyzing powers at 3° are mainly related to $1f_{5/2}$ contributions. Fits of comparable quality were achieved using the other background options discussed in Sec. III B and for ^{119}Sn.

No dependence of theoretical observables with excitation energy was taken into account in the above standard analysis. The separation energy dependence of $1g_{9/2}$, $1f_{5/2}$, and $1f_{7/2}$ form factors due to the coupling with surface vibrations was taken into account in a second analysis (hereafter QPMFF analysis) following the procedure described in details in Ref. [34]. The mean source term entering the inhomogeneous equations, as calculated in the QPM model, was found of first-derivative Woods-Saxon shape and located 0.3 fm inside the well radius. The form factors calculated at several excitation energies with the code of Ref. [33] were used in DWBA calculations. The angular distribution shapes of the observables σ, A_y, and A_{yy} deduced in this QPMFF ap-

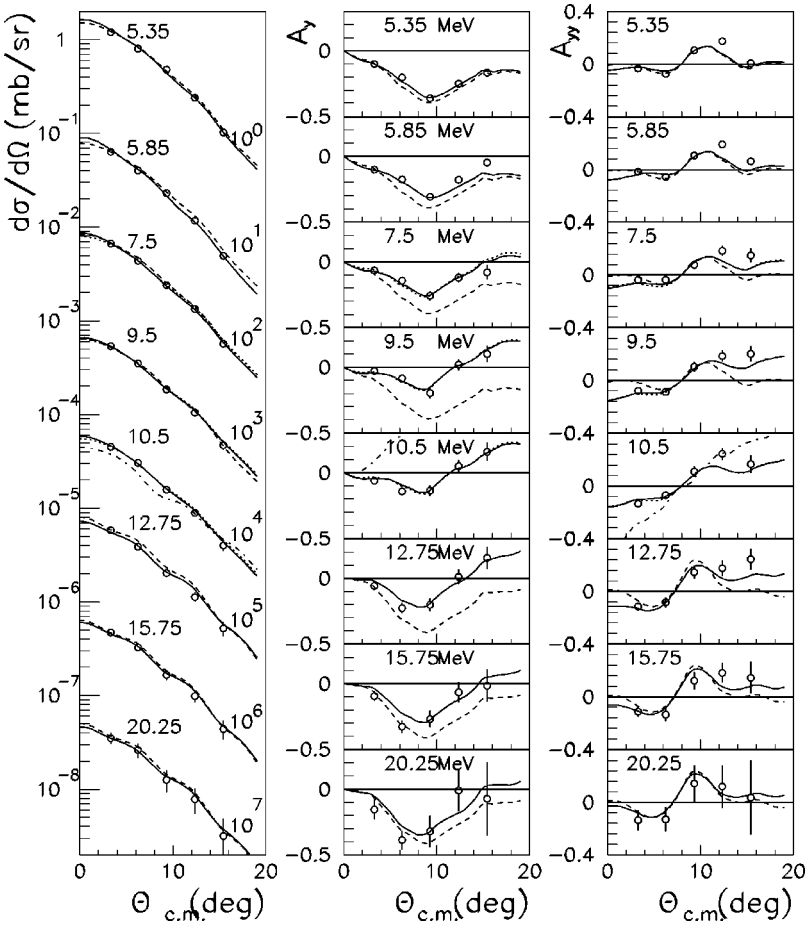

FIG. 4. Typical angular distributions of cross sections and analyzing powers corrected for the background (see text and Sec. III B) and deep hole contribution. The mean excitation energy of each bin is indicated on the figure. Solid lines: best fit angular distributions. Dotted lines: fits obtained with $g_{9/2}$ and $f_{5/2}$ only between 6 and 12 MeV. Dashed lines: angular distributions of pure $1g_{9/2}$ (for the four lower excitation energy bins) or $1f_{7/2}$ (for the three higher energy bins) transitions. Dashed-dotted lines: angular distributions of a $1f_{5/2}$ transition.

proach were found nearly insensitive to excitation energy, within several MeV, as previously shown in the case of ^{208}Pb [34]. As a consequence, the QPMFF and standard analyses only differ by the extracted spectroscopic strengths $\mathcal{S}_i$.

The ratios $R_{\mathcal{S}}(E_X)$ of QPMFF spectroscopic strengths to standard spectroscopic strengths are shown in Fig. 5. We have considered the range of excitation energies giving stable angular distribution shapes as the one of interest for the fragmentation. As shown in Fig. 5, the dependence of $S_{\mathcal{S}}$ on E_X is much stronger for the $1f$ holes than for the $1g_{9/2}$ hole state.

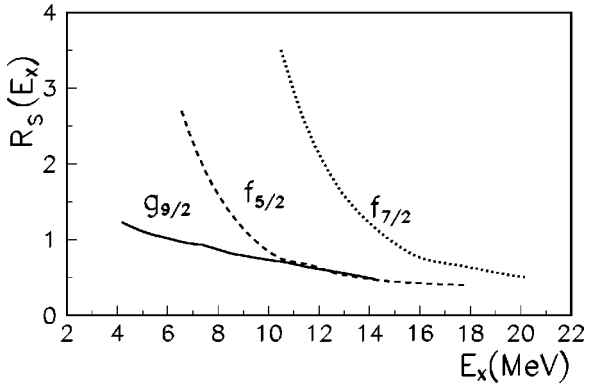

FIG. 5. Ratios $S_{\mathcal{S}}(E_X)$ of QPMFF to standard spectroscopic strengths for the $1g_{9/2}$, $1f_{5/2}$, and $1f_{7/2}$ inner hole states.

B. The background of multistep reactions

Collective excitations are expected to play a dominant role in inelastic scattering steps involved in two-step or multistep (d,t) reactions at 200 MeV in the forward angle region. Coupled channel calculations of two-step cross-section spectra and vector and tensor dependent spectra were performed for the ^{116}Sn target following the procedure described in detail in Ref. [34] for ^{208}Pb. Transitions with multipolarities $L \leqslant 3$ were taken into account. The characteristics adopted for the main low-lying collective transitions and for the dipole, quadrupole and octupole giant resonances, taken from Refs. [41,42], are shown in Table I. A limitation of the procedure, which is time consuming, is the large number of independent calculations needed, which increases with mul-

TABLE I. Characteristics of low multipolarity collective excitations used in multistep and coupled channel calculations.

Low lying phonons			Giant resonances			
J^π	E_X (MeV)	β	Resonance	E_X (MeV)	β	Width (MeV)
2^+	1.29	0.1	GDR	15.8	0.22[a]	5.0
3^-	2.27	0.11	GQR	13.4	0.12	3.8
4^+	2.7	0.09	LEOR	6.5	0.12	2.7
5^-	3.7	0.06	HEOR	23.0	0.1	7.0

[a]Coulomb excitation for Coulomb inelastic scattering.

tipolarity of inelastic transitions. Multistep contributions at 200 MeV are expected to also involve $L \geqslant 4$ multipolarities and three or even high-order step pickup.

The Feshbach, Kerman, and Koonin model of multistep reactions [43], (hereafter FKK), has been successfully used to describe multistep reactions over wide ejectile angular and energy ranges. The FFK model enables the continuum cross section to be expressed as an incoherent sum of one-step and multistep cross sections. The leading-particle statistical assumption allows an expression of the second and higher-step cross sections in a compact and recursive form, requiring as input first-order DWBA cross sections only, in order to calculate *n*-step cross-section spectra from the $(n-1)$-step cross-section results. The calculation code developed by Koning and Akkermans [35], based on the FKK model, was adapted to the description of the multistep (d,t) reaction at intermediate energy. The procedure and details have been described in Ref. [44].

It is assumed that the pickup transition occurs at the first step of the reaction and inelastic transitions at the second- and higher-order steps, so that triton cross sections could be entered as independent inputs in the modified code. All inner and deep hole contributions to triton spectra are described using Gaussian-type energy distributions. Valence level contributions are weighted by the spectroscopic strengths and slightly spread.

The contribution of collective excitations to inelastic steps in such multistep direct calculations (hereafter MSD) is described in Eq. (2). DWBA inelastic cross sections calculated with a macroscopic form factor taken as the triton derivative potential are weighted by excitation energy dependent strength distributions.

$$\frac{d^2\sigma^{(1)}(E,\Omega \leftarrow E_{n-1},\Omega_{n-1})}{d\Omega\, dE} = \sum_L \frac{d\beta_L^2(E_X)}{dE}\left[\frac{d\sigma^{(1)}(E,\Omega \leftarrow E_{n-1},\Omega_{n-1})}{d\Omega}\right]_L^{DWBA}. \tag{2}$$

E,Ω refers to the triton energy and solid angle, E_X is the nucleus excitation energy change. Collective strength distributions $d\beta_L^2(E_X)/dE$ corresponding to the low-lying collective excitations and to the $L \leqslant 3$ giant resonances were calculated with the energies, β values and widths given in Table I. Evidence for higher multipolarity giant resonance is not as well established. We have assumed that $\sim 60\%$ of each of these collective strengths would be spread around $L\hbar\omega$ and higher excitation energies were added to approximately exhaust the sum rule up to $E_X = 100$ MeV.

Two-step MSD spectra calculated at 3° in ^{115}Sn for quadrupole and octupole collective excitations are compared in Figs. 6(a) and 6(b) with the coupled channel results. A fairly good agreement is achieved for the two multipolarities, with the same strength renormalization parameter in MSD calculations. An excitation energy dependent correction to two-step angular distributions was applied in MSD calculations, as suggested by the too small slope calculated in a low excitation energy range (1.1–3.7 MeV) known to be mainly populated by two-step pickup [19,45].

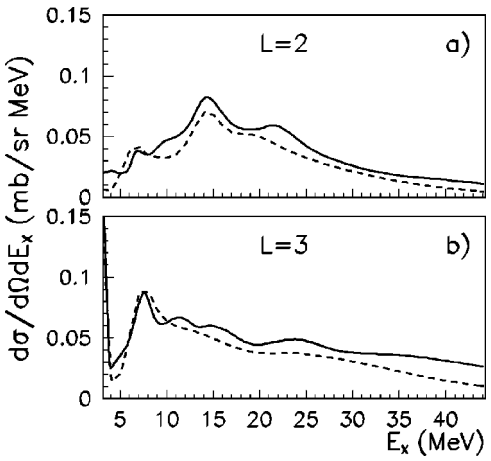

FIG. 6. Coupled channel (solid curves) and MSD (dashed curves) two-step cross sections at 3° in ^{115}Sn for $L=2$ and $L=3$ collective excitations.

Multistep calculations were performed up to six steps in both nuclei, taking into account inelastic transitions with multipolarities up to $L=8$. The background cross-section spectra referred to as back1 are obtained assuming that collective excitations dominate inelastic steps for all multipolarity transitions. The description of back2 takes into account collective excitations only for multipolarities $L \leqslant 3$. Higher multipolarity transitions are assumed to excite many levels, as described via a level density formula. Both calculations were performed in ^{116}Sn with the strength normalization parameter determined by comparison with two-step coupled channel results. Fair agreement with the data at high excitation energy are achieved, as shown Fig. 1. No coupled channel calculations were performed in the case of ^{119}Sn. The MSD calculations were performed with the same collective excitation characteristics as for ^{115}Sn, a reasonable assumption for the present purpose. The MSD parameter was adjusted to reproduce the cross section measured at 15° for the 43 MeV excitation energy bin. It is found 7% smaller than in ^{115}Sn, a difference quite acceptable.

The present MSD calculations give no information on the background analyzing powers. These analyzing powers were calculated in the region of interest from the data obtained at high excitation energy, which are dominated by background contributions. Three excitation energy bins 7 MeV wide and centered at 27 MeV, 35 MeV, and 43 MeV, respectively, were considered.

The total background analyzing powers in the high excitation energy bins are fairly well determined by subtracting from the data the small calculated contribution of one-step pickup populating inner and deep hole states. The three angular distributions shown in Fig. 7(a) are very similar, within error bars. Extrapolating this behavior, the total background analyzing powers were assumed to be reasonably described at all excitation energies by the mean curves shown as backa in Fig. 7(a).

In a second approach, two groups of background contributions were considered separately and added in Eqs. (1):

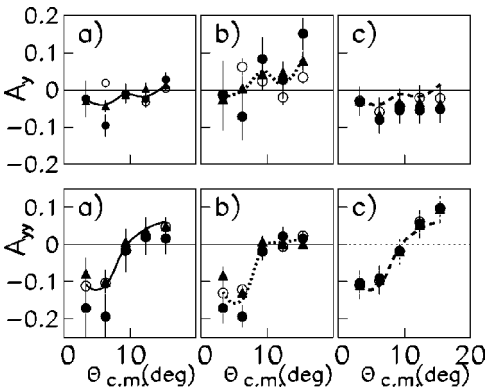

FIG. 7. Background vector and tensor analyzing powers angular distributions. (a) Analyzing powers backa, inner hole contributions subtracted. Filled dots: $E_X=27$ MeV. Triangles: $E_X=35$ MeV. Circles: $E_X=43$ MeV. Solid lines: analyzing powers angular distributions averaged over the three excitation energy bins. (b) Residual background analyzing powers (see text), inner hole and $L=1-3$ two-step contributions subtracted. Filled dots, triangles, circles, and solid line as in (a). Dotted lines: analyzing powers angular distributions averaged over the three excitation energy bins. (c) Analyzing powers backb, calculated at 7.5 MeV (filled dots), 10.5 MeV (triangles), and 14.25 MeV (open circles). See text. Dashed lines: angular distributions of analyzing powers averaged over the three excitation energy bins.

The group of two-step pickup contributions involving multipolarity transitions $L=1-3$, as given by coupled channel calculations, and the contribution of a residual background corresponding to all other multistep processes. This latter one was calculated in the high excitation energy bins by subtracting from the data the above mentioned $L=1-3$ two-step contributions together with the one-step pickup ones [see Fig. 7(b)]. No significant dependence on excitation energy is observed, suggesting that the average curves of Fig. 7(b) would reasonably describe the residual background at lower excitation energies. Typical angular distributions of the total background analyzing powers deduced in this second approach are shown as backb in Fig. 7(c). They compare rather well with the first approach results, except for somewhat larger values of tensor analyzing powers at the largest angles.

IV. RESULTS AND DISCUSSION

Experimental histograms of the $1g_{9/2}$, $1f_{5/2}$, and $1f_{7/2}$ strengths in ^{115}Sn and ^{119}Sn were built with the standard and QPMFF spectroscopic strengths extracted in each bin as explained in Sec. III A. Examples of the dependence of $1f_{5/2}$ and $1f_{7/2}$ histograms in ^{115}Sn on background calculation options are shown in Fig. 8. The $1f_{7/2}$ results (and also the $1g_{9/2}$ ones) change only by few %. Larger effects are observed for the $1f_{5/2}$ hole due to its smaller cross sections and its concentration in a region where background observables depend most on the chosen option (see Fig. 1). All results in the following refer to the histograms obtained with background cross section and analyzing power options back1 and backa, respectively.

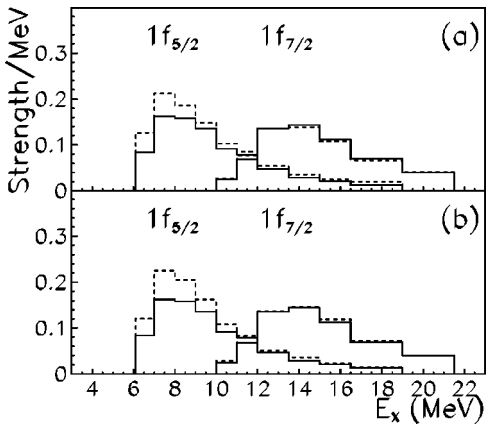

FIG. 8. Dependence of $1f_{5/2}$ and $1f_{7/2}$ QPMFF strength histograms on the background option (see Sec. III B). Solid lines: cross section back1 and analyzing power backa. (a) Dashed lines: with cross section back2 and analyzing powers backa. b) Dashed lines: with cross section back1 and analyzing powers backb.

All histograms are strongly asymmetric, with a high excitation energy tail. They were fitted with Gaussian-type curves, a method adopted in Refs. [34,46], in order to determine the quasihole energies and the spreading widths, discussed later on.

A. Comparison with previous experimental results

None of the previous experiments on tin nuclei had been analyzed taking into account the form factor modifications induced by the coupling of quasiparticle states with collective configurations. The standard analysis results were consequently chosen for consistency in the following comparison with previous data.

Integrated strengths in the $1g_{9/2}$ main structure and the tail in ^{115}Sn are compared in Table II with results of Refs. [8,15,17,20]. Spectroscopic strengths given for these latter work, deduced of the spectroscopic factors given in the references, were interpolated when necessary from results corresponding to slightly different excitation energy bins from those considered in the table. A good or fairly good agreement is achieved for the structure, especially with Refs. [15,20]. The $1g_{9/2}$ tail strength in the present experiment is in good agreement with the values given in Refs. [8,20] and compatible with the upper limit given in Ref. [15]. These latter authors notice that the vector analyzing power in the structure tail is somewhat better described by the combina-

TABLE II. Experimental integrated $1g_{9/2}$ strength $\mathcal{S}$ in ^{115}Sn energy bins $\Delta(E_X)$.

	$(\vec{d},t)$	$(\vec{d},t)$	$(^3\mathrm{He},\alpha)$	$(^3\mathrm{He},\alpha)$	(p,d)
$\Delta(E_X)$	200 MeV	50 MeV	39 MeV	283 MeV	50 MeV
(MeV)	This work	Ref. [15][a]	Ref. [17]	Ref. [20][a]	Ref. [8][a]
3.6–6.5	0.58	0.55	0.46	0.56	0.52
6.5–10.5	0.35	(0.40)[b]		0.35(0.42)[b]	0.38[b]

[a]Adjusted to energy bin differences.

[b]Value within parentheses: With no $l=3$ contribution.

TABLE III. Experimental integrated $1g_{9/2}$ strength $\mathcal{S}$ in ^{119}Sn energy bins $\Delta(E_X)$ in MeV.

This work	Ref. [17]	Refs. [6,7]	Ref. [8]
$\Delta(E_X)$ $\mathcal{S}$	$\Delta(E_X)$ $\mathcal{S}$	$\Delta(E_X)$ $\mathcal{S}$	$\Delta(E_X)$ $\mathcal{S}$
4.3–6.5 0.51	4.3–6.5 0.25	4.3–6.6 0.22	3.9–6.5 0.51
6.5–10.2 0.33			6.5–10.2 0.35

tion of $2p$ and $1f_{5/2}$ contributions than by $2p$ and $1g_{9/2}$ ones.

As shown in Table III, the integrated $1g_{9/2}$ strength in the ^{119}Sn structure and tail in the present work is in good agreement with Ref. [8]. The smaller strengths given for the structure in Refs. [6,7,17] may be attributed to notably larger background to peak cross-section ratios.

Integrated $1f_{5/2}$ and $1f_{7/2}$ strengths in ^{115}Sn are shown in Table IV. The upper limits given in Ref. [15] are, as expected, larger than the present values, and the indicative values of Ref. [20] are in fair agreement with the present data.

The ^{115}Sn and ^{119}Sn spectrum shapes observed in different experiments deserve an additional comment. The rather wide bump observed in the (d,t) reaction at $E_d=40$ MeV [9], below and beyond the $1g_{9/2}$ peak is clearly assigned mainly to the $l=1$ strength. A bump, $\sim$1.3 MeV beyond the $1g_{9/2}$ peak, observed via the $(^3\mathrm{He},\alpha)$ reaction at $E_d=110$ MeV in several tin isotopes [18] and a similar feature suggested in Ref. [20] have been attributed to the $1g_{9/2}$ strength. A possible secondary bump in the ^{119}Sn spectra populated via the $(p,\vec{d})$ reaction at 90 MeV [6,7] does not exhibit a $1g_{9/2}$ signature. A shoulder, more pronounced at 15° than at 3° is also observed in both tin nuclei in the present work. We attribute this shoulder mainly to the background shape, as shown in Figs. 1 and 2. Calculations of two-step cross sections in the other reactions would be necessary for a further comparison.

B. Experimental and theoretical strength distributions

The coupling of single particle degrees of freedom with the surface modes has long been recognized to play a decisive role in strength fragmentation. Most theoretical approaches have treated this coupling via microscopic calculations.

The calculations of Koeling and Iachello [28] describe the fragmentation of the $1g_{9/2}$ strength in tin isotopes in term of a doorway-state-like picture. The hole strength is first fragmented due to the strong coupling to the first collective 2^+ and 3^- levels. The fragments are subsequently spread over the many underlying noncollective states in a statistical way. Average matrix elements and density of 3 and 5 quasiparticle states involved in this description are taken into account. The calculations predict much too strong concentration of the $1g_{9/2}$ strength.

TABLE IV. Experimental integrated $1f_{5/2}$ (top) and $1f_{7/2}$ (bottom) strengths $\mathcal{S}$ in ^{115}Sn.

This work		Ref. [15]		Ref. [20]	
$\Delta(E_X)$	$\mathcal{S}$	$\Delta(E_X)$	$\mathcal{S}$	$\Delta(E_X)$	$\mathcal{S}$
7.4–10.6	0. 39	7.4–10.6	0.93 [a]	8.6-11.6	0.58
10.6–19.0	0.53	10.6–19.4	1.43 [b]	11.6–18.5	0.35
11.6–18.5	0.79	10.6–19.4	0.60	11.6–18.5	1.17

[a]Without $l=4$ contribution.

[b]Without $1f_{7/2}$ contribution.

The results of Vdovin [49], calculated in the framework of the QPM model, supersede those previously published by the Dubna group [25,30,31]. The model contains an average field described by a Woods-Saxon well, complemented by pairing interactions and separable multipole and spin multipole forces. The radial shape of the corresponding long range interaction is taken as the first derivative of the central well, instead of the r^λ shape adopted in different older calculations. A standard parameter set, acceptable in a large range of nuclei is used, instead of parameter sets depending on each nucleus. The coupling with $|1qh\otimes 1ph\rangle$ and $|1qh\otimes 2ph\rangle$ configurations involving phonons of multipolarity up to $L=7$ including the giant-resonance region is taken into account, as in previous calculations. Uncertainties on excitation energies are estimated $\sim$300 keV in such calculations.

Bortignon and Broglia [29] calculate the $1g_{9/2}$ strength distribution in ^{119}Sn, using Hartree-Fock wave functions and energies predicted with the Skyrme III force, together with a surface effective interaction of first derivative Woods-Saxon potential shape. Calculations are performed in the space of $|1qh\otimes 1ph\rangle$ configurations, taking into account natural parity collective levels and giant resonances. The particle-hole force strength is adjusted to fit the lowest 2^+ level energy in ^{120}Sn.

All the above theoretical calculations simulate the coupling to more complex configurations, not taken into account explicitly, by distributing the strength using a Lorentzian distribution, with the width as smearing parameter.

The $1g_{9/2}$ strength function has been calculated with similar semimicroscopic approaches in Ref. [47] and later on in Ref. [48], within the optical phonon model (OPM). The coupling of a hole state with a background of noncollective many-particle-many-hole states is described in these models via a phenomenological imaginary optical potential.

1. The $1g_{9/2}$ strength

Experimental and theoretical responses are compared in Figs. 9 and 10, respectively, for ^{115}Sn and ^{119}Sn. Integral characteristics are shown in Table V. The two experimental responses are rather similar except for the stronger peaking at 5.35 MeV in ^{115}Sn. This latter characteristic is attributed in Ref. [28] to an especially small density of $9/2^+$ levels in the ^{115}Sn peak excitation energy region.

QPM calculations predict fairly well the $1g_{9/2}$ quasihole energy in ^{115}Sn and ^{119}Sn, as shown in Table V. Theoretical histograms derived using the same bin widths as in the experiment from two phonon QPM distributions ([49]2ph in Table V) compare rather well with the data at the peak maximum, as shown in Figs. 9 and 10. It should be remarked that the identification of a small amount of $1g_{9/2}$ strength predicted at very low excitation energy was not attempted in the present experiment.

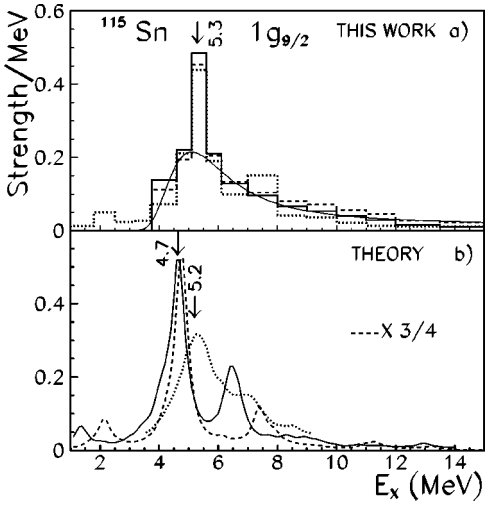

FIG. 9. Experimental and theoretical $1g_{9/2}$ neutron hole strength distributions in ^{115}Sn. (a) Solid line: histogram of the experimental strength deduced with the QPMFF analysis. Dashed line: with the standard analysis. Dotted line: QPM histogram shifted to the experimental peak position. Thin solid line: Gaussian-type distribution with 85% of the experimental strength. (b) Solid lines: QPM strength distribution [49] calculated with up to $|1qh\otimes 2ph\rangle$ configurations. Dashed line: QPM strength distribution calculated for $|1qh\otimes 1ph\rangle$ components only, multiplied by 0.75 for convenience. Dotted line: OPM theoretical strength distribution of Ref. [48].

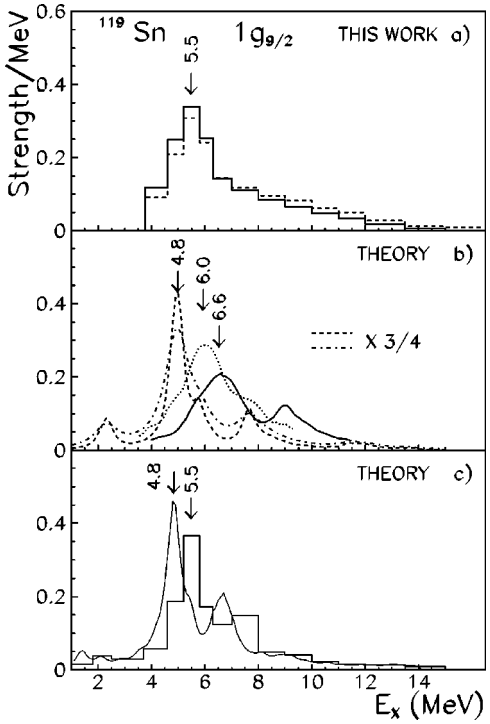

FIG. 10. Experimental and theoretical $1g_{9/2}$ neutron hole strength distributions in ^{119}Sn. (a) Solid and dashed histograms as in Fig. 9, respectively. (b) Solid line: Calculations of Ref. [29]. Dashed and dash-dotted lines: QPM calculations [49] with $|1qh\otimes 1ph\rangle$ components only and smearing parameter 0.5 MeV and 1 MeV, respectively. The dashed curve was reduced to 0.75 of calculated values for convenience. Dotted line: OPM calculation of Ref. [48]. (c) Solid lines: QPM calculations with $|1qh\otimes 2ph\rangle$ components and corresponding histogram shifted to reproduce the experimental peak position.

The calculations of Ref. [29] in ^{119}Sn are not expected to reproduce the $1g_{9/2}$ peak position. They underestimate significantly the maximum strength per MeV. The strength distribution of Ref. [29] is compared in Fig. 10(b) with a QPM strength distribution calculated within the $|1qh\otimes 1ph\rangle$ approximation with the smearing parameter $\Delta=1$ MeV used in Ref. [29] (instead of 0.5 MeV in Ref. [49]). The remaining difference between the two distributions suggests that the coupling interaction is somewhat stronger in Ref. [29] than in Ref. [49], and possibly too strong.

Both the calculations of Refs. [29,49] predict a secondary peak $\sim$1.8 MeV beyond the main structure, which is not observed in the experiments. They do not reproduce either the significant high excitation energy tail. These latter features are better reproduced by the OPM model of Ref. [48], as shown in Figs. 9 and 10, but the OPM model overestimates somewhat the damping in the structure region.

2. The $1f_{5/2}$ strength

The experimental distributions are very similar in ^{115}Sn and ^{119}Sn (see Figs. 11 and 12). The strength distributions deduced via the QPMFF and the standard analyses are strikingly different. As shown in Table VI, the QPMFF analysis shifts the centroids and quasihole energies downwards and leads to much smaller spreading widths.

QPM calculations performed with $|1qh\otimes 1ph\rangle$ configurations only, lead to strongly structured strength distributions in contradiction with the data. The more complete calculations including $|1qh\otimes 2ph\rangle$ configurations improve significantly the predictions. Nevertheless, the theoretical strength distributions are only slightly asymmetric and the theoretical spreading widths are much too small compared even with QPMFF widths. Increasing the smearing parameter (0.5 MeV in the calculations of Ref. [49]) would reduce the maximum strength per MeV in better agreement with the data, without spreading enough the strength towards higher excitation energies. The QPMFF spreading width is quite well reproduced by the semiempirical formula used for deep hole state spreading, calculated at the experimental quasihole energy.

3. The $1f_{7/2}$ strength

Experimental strength distributions are shown in Figs. 13 and 14 and integral characteristics are presented in Table VII. The smooth overlap of $1g_{9/2}$ and $1f_{7/2}$ strengths from 10 MeV to 15 MeV in ^{115}Sn was shifted upwards in ^{119}Sn by $\sim$0.5 MeV (a value consistent with Hartree-Fock predictions). Uncertainties in these overlaps may induce significant errors on the low excitation energy side of the $1f_{7/2}$ strength distributions. Additional checks have shown that a shift downwards of the overlaps significantly exceeding 0.6 MeV would not be acceptable.

The experimental $1f_{7/2}$ strength distributions are found somewhat different in ^{115}Sn and ^{119}Sn, as shown in Figs. 13 and 14, in spite of rather large errors due to the subtraction of

TABLE V. Integral characteristics of the $1g_{9/2}$ strength distributions in ^{115}Sn (top) and ^{119}Sn (bottom). E_X^{min} and E_X^{max} are the excitation energy limits. E_X^{qh}, E_X^c, and $\Gamma\downarrow$ are the quasihole excitation energy, the centroid energy and the spreading width. Experimental values without and with parentheses are derived, respectively, from the QPMFF and standard analyses.

	E_X^{min} (MeV)	E_X^{max} (MeV)	E_X^{qh}[a] (MeV)	E_X^c (MeV)	$\mathcal{S}$	$\Gamma\downarrow$[a] (MeV)
This work[b]	3.75	15.0	5.15[c] [5.35]	6.65 (7.2)	1.01 (1.06)	2.2,[c] [5.4] [6.1]
Theory[d]						
Ref. [49]2ph	3.1	14.3	[4.65]	5.75	0.89	[4.8]
This work[b]	3.75	15.0	5.35 [5.5]	6.75 (7.25)	1.09 (1.11)	2.3 [5.2] [6.0]
Theory[d]						
Ref. [49]2ph	3.1	14.3	[4.8]	6.2	0.88	[5.0]
Ref. [29]	4.0	12.7	[6.6]	7.6	0.8	[4.3]

[a]Experimental quasihole energies and spreading widths correspond to Gaussian-type fits. The values within square brackets are the main peak energies and the Gaussian widths derived from the variances σ.

[b]Assuming a smooth overlap with the $1f_{7/2}$ strength from $E_X=10$ to 15 MeV (10.5–15.5 in ^{119}Sn).

[c]The ^{115}Sn experimental quasihole energies and spreading widths take into account the Gaussian-type distribution shown in Fig. 9, corresponding to 85% of the experimental strength and the 5.35 MeV peak rising on it.

[d]Theoretical energy limits take into account the shift between the theoretical and experimental distributions.

large background contributions. The smaller integrated strength in ^{119}Sn than in ^{115}Sn shown in Table VI is partly accounted for by a slightly smaller excitation energy range, the integrated strengths being fairly consistent with the spreading widths in both isotopes. It is tempting to relate the difference between the two $1f_{7/2}$ histograms to the observation of a clear bump in ^{115}Sn spectra at the most forward angles, which is missing in ^{119}Sn (see Figs. 1 and 2). One may remark that the background exhibits a smooth maximum around $E_X=15.2$ MeV in ^{115}Sn, very near the $1f_{7/2}$ cross section maximum. One would not exclude in this bump small residual contributions of one- and two-step interference terms, which are generally expected to cancel over 1 MeV energy bins. The dominant contribution of two-step pickup involving the valence levels and the giant quadrupole resonance to the above feature at 3° may be expected at somewhat lower excitation energy in ^{119}Sn, while the $1f_{7/2}$ cross section maximum is observed at slightly higher excitation energy. QPMFF quasihole and centroid energies are shifted downwards compared with the standard analysis values. The extracted spreading widths are strongly reduced by taking into account the form factor energy dependence.

QPM distributions calculated with only $|1qh\otimes 1ph\rangle$ components are rather similar to those including also $|1qh\otimes 2ph\rangle$ components [see Figs. 13(b) and 14(b)]. The predicted quasihole positions are much lower than those deduced from the experiment even via the QPMFF analysis.

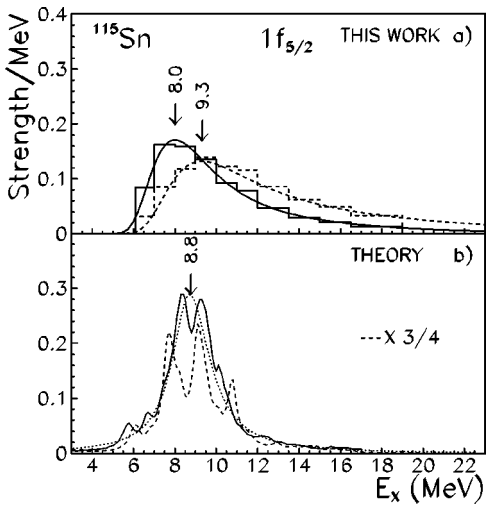

FIG. 11. Experimental and theoretical $1f_{5/2}$ neutron hole strength distributions in ^{115}Sn. (a) Solid and dashed histograms as in Fig. 9. Solid and dashed curves: Gaussian-type fits to the QPMFF and standard strength distributions, respectively. (b) Solid and dashed curves as in Fig. 9(b). Dotted curve: Fit of the $|1qh\otimes 2ph\rangle$ QPM strength distribution with a Lorentzian shape.

The spreading widths predicted in Ref. [49] with a smearing parameter of 1 MeV are the same in both isotopes and only 50–60 % of those deduced from the experiment.

One may note that the widths obtained with the semiempirical formula of Ref. [27] and the parameters used for deep hole states are typically ~20% larger than the QPMFF spreading widths shown in Table VII.

C. Discussion

Important qualitative features of experimental strength distributions in ^{115}Sn and in ^{119}Sn are still not well explained by the existing theoretical calculations. Technical limitations involved in QPM calculations (such as violations of the Pauli principle or the neglect of phonon-phonon interactions), dis-

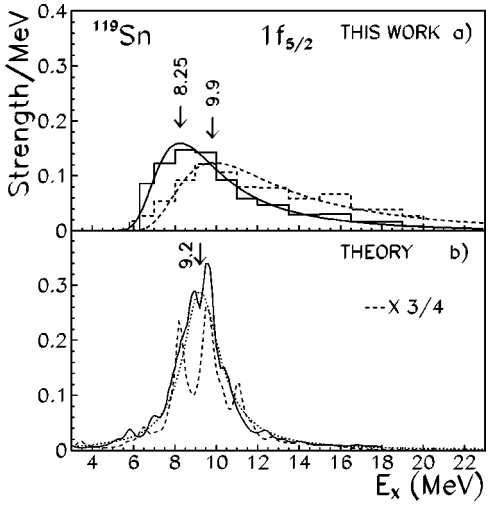

FIG. 12. Experimental and theoretical $1f_{5/2}$ neutron hole strength distributions in ^{119}Sn. Histograms and curves as in Fig. 11.

TABLE VI. Integral characteristics of the $1f_{5/2}$ strength distributions in ^{115}Sn (top) and ^{119}Sn (bottom). E_X^{min}, E_X^{max}, E_X^{qh}, E_X^c and $\Gamma\downarrow$ and experimental values defined as in Table V.

	E_X^{min} (MeV)	E_X^{max} (MeV)	E_X^{qha} (MeV)	E_X^c (MeV)	$\mathcal{S}$	$\Gamma\downarrow^a$ (MeV)
This work	6.1	19.0	8.0	10.0	0.89	3.6 [6.6]
			(9.3)	(11.5)	(0.99)	(5.2)
Theory[b]						
Ref. [49]2ph	6.9	19.8	8.8	9.3	0.91	2.2 [4.4]
This work	5.8	20.0	8.25	10.4	0.89	3.7 [7.2]
			(9.8)	(12.2)	(0.97)	(5.5)
Theory[b]						
Ref. [49]2ph	6.8	21.0	9.2	9.7	0.89	2.2 [4.4]

[a]Experimental quasihole energies and spreading widths correspond to the Gaussian-type fits. Theoretical values correspond to Lorentzian type fits. The values within [ ] are the Gaussian widths derived from the variances σ.

[b]Theoretical energy limits take into account the shift between the theoretical and experimental distributions.

cussed in Ref. [1], are expected to be of limited importance. More severe truncations of the configuration space generally needed in calculations involving $|1qh\otimes 2ph\rangle$ components, while changing strength distribution shapes, would have little effects on the distribution moments. A larger coupling strength would increase the $1f$ spreading widths. More specifically, the coupling strengths needed for high excitation energy phonons would be larger than those involved in the $1g_{9/2}$ calculations, which fairly well reproduce the maximum strength per MeV. Neglected effects, such as the coupling with higher-order configurations or higher-order terms in the interaction, are not correctly simulated by a smearing parameter independent of excitation energy. The fact that the secondary peaks predicted beyond the main $1g_{9/2}$ structure both in Refs. [49] and [29] are not observed experimentally sup-

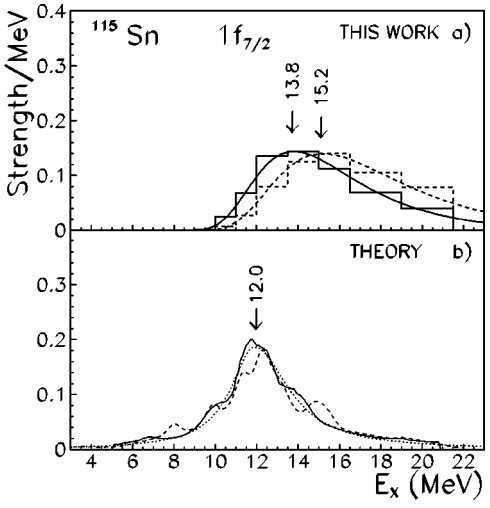

FIG. 13. Experimental and theoretical $1f_{7/2}$ neutron hole strength distributions in ^{115}Sn. (a) Histograms and curves as in Fig. 11. (b) Solid and dotted curves as in Fig. 11. Dashed curves: QPM calculations [49] with $|1qh\otimes 1ph\rangle$ components.

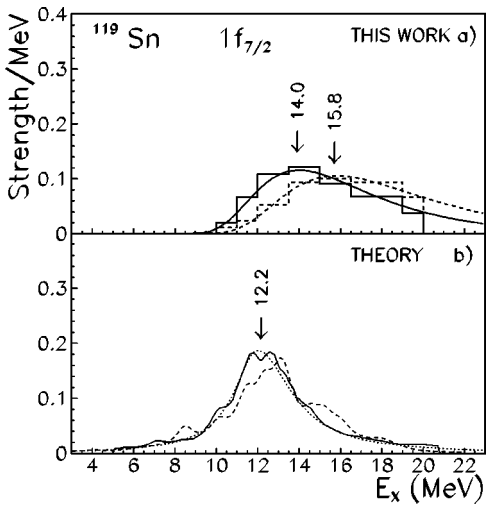

FIG. 14. Experimental and theoretical $1f_{7/2}$ neutron hole strength distributions in ^{119}Sn. (a) Histograms and curves as in Fig. 13. (b) Solid, dashed, and dotted curves as in Fig. 13.

ports this conclusion, which is also suggested by the smooth $1f$ strength high excitation energy tail.

The increase of level densities with excitation energy may be responsible for larger spreading effects at high excitation energy than predicted by theoretical calculations using a constant smearing parameter. Doll [50] in particular has successfully described $1d_{5/2}$ proton hole strength distributions in nuclei around $A=40$ by using a smearing parameter proportionnal to the level density. Level densities increase much more rapidly with excitation energy in tin nuclei. Our attempts to improve over the present theoretical predictions in tin nuclei following this procedure were not consistently successful. This points to the need of an improved theoretical description of the hole coupling with many quasiparticle states.

TABLE VII. Integral characteristics of the $1f_{7/2}$ strength distributions in ^{115}Sn (top) and ^{119}Sn (bottom). E_X^{min}, E_X^{max}, E_X^{qh}, E_X^c and $\Gamma\downarrow$ and experimental values defined as in Table V.

	E_X^{min} (MeV)	E_X^{max} (MeV)	E_X^{qha} (MeV)	E_X^c (MeV)	$\mathcal{S}$	$\Gamma\downarrow^a$ (MeV)
This work[b]	10.0	21.5	13.8	15.2	0.93	5.8 [6.3]
			(15.2)	(16.4)	(1)	(7.1)
Theory[c]						
Ref. [49]2ph	8.5	20.0	12.0	12.6	0.85	3.4 [5.4]
This work[b]	10.0	20.0	14.0	14.9	0.83	6.5 [5.5]
			(15.8)	(16.0)	(0.76)	(8.0) [5.2]
Theory[c]						
Ref. [49]2ph	8.7	18.7	12.2	12.8	0.82	3.4 [4.9]

[a]Experimental quasihole energies and spreading widths correspond to the Gaussian-type fits. Theoretical values correspond to Lorentzian type fits. The values within [ ] are the Gaussian widths derived from the variances σ.

[b]Assuming a smooth overlap with the $1g_{9/2}$ strength.

[c]Theoretical energy limits take into account the shift between the theoretical and experimental distributions.

TABLE VIII. Relative positions in MeV of excitation energy centroids in ^{115}Sn.

	H.F. SKIII Ref. [39]	QPM Ref. [49]	EXPERIMENT QPMFF	EXPERIMENT Standard
$1f_{7/2}$-$1g_{9/2}$	9.1	6.85	8.55	9.2
$1f_{7/2}$-$1f_{5/2}$	4.4	3.3	5.2	4.9

Significant discrepancies between experiment and QPM predictions bear on the relative location of the $1g_{9/2}$, $1f_{5/2}$ and $1f_{7/2}$ centroids, as shown in Table VIII for ^{115}Sn. The QPM $1f_{7/2}-1g_{9/2}$ gap and the $1f_{7/2}-1f_{5/2}$ spin-orbit splitting are significantly smaller than found experimentally. Both are scaled down by a factor ~ 0.75 compared with Hartree-Fock predictions obtained with the Skyrme III force, which reproduce somewhat better the data.

QPMFF strength distributions depend critically on the form factor modifications induced by the hole coupling with surface vibrations. The surface localization of the interaction is most important in this respect. In the limiting and unrealistic assumption of no correlation of particle-hole states, strength distributions would not differ much from the standard ones, as indicated by calculations performed in the case of ^{207}Pb [51].

V. SUMMARY AND CONCLUSIONS

We have studied the highly excited neutron hole states in ^{115}Sn and ^{119}Sn via the $(\vec{d},t)$ reaction at $E_d=200$ MeV. Experimental spectra were measured up to $E_X=45$ MeV and $E_X\sim 21$ MeV in ^{115}Sn and ^{119}Sn, respectively, from 3° to 15°. The measurement of three observables (differential cross section, vector, and tensor analyzing powers) has allowed the determination of the $1g_{9/2}$, $1f_{5/2}$, and $1f_{7/2}$ inner hole strength distributions up to $E_X=21.5$ MeV in ^{115}Sn and 20 MeV in ^{119}Sn.

Special efforts have been made to calculate the background of multistep pickup, to calibrate it at high excitation energy and to correct for it. The multistep cross section spectra have been calculated for the first time for two-step and higher-order step pick-up, using the multistep code of Ref. [35], modified to take into account successive collective excitations. Cross sections and analyzing powers of two-step pickup involving low multipolarity collective excitations have been obtained for ^{115}Sn via coupled channel calculations. Good agreement of MSD cross sections with coupled channel results is achieved for two-step pickup involving either quadrupole or octupole collective excitation, with a same parameter renormalizing collective strengths. ^{119}Sn spectra measured at 15° around $E_X=43$ MeV allowed the background calibration.

The hole coupling with surface vibrations, expected to be responsible of the main features of the studied hole fragmentation, was taken into account for the first time in the description of hole form factors in tin nuclei used in DWBA analyses. Form factors were calculated in the framework of the QPM model, following the procedure developed for neutron holes in ^{207}Pb. The $1f_{5/2}$ and $1f_{7/2}$ QPMFF strength distributions extracted with this refined analysis are strikingly shifted downward in comparison with the distributions extracted with the standard analysis, and their spreading widths are $\sim 25\%$ smaller.

The present results complement our knowledge of the $1g_{9/2}$ strength in ^{115}Sn and ^{119}Sn beyond the main structure. $1f_{5/2}$ and $1f_{7/2}$ strength distributions are obtained for the first time in the excitation energy region where indications of them were previously found. The $1f_{5/2}$ strength distributions are found very similar in both isotopes, except for a slight upward energy shift in ^{119}Sn. This is not the case of the $1f_{7/2}$ strength distributions, a difference possibly linked to small contributions of one step and two-step interference terms to the $E_X=14.5$ MeV bump observed in ^{115}Sn spectra.

The $1g_{9/2}$, $1f_{5/2}$, and $1f_{7/2}$ strength distributions exhibit a more or less pronounced peak or bump and a smoothly decreasing high excitation energy tail. Quasihole energies and spreading widths have been deduced from Gaussian-type fits of the strength histograms, a method used for neutron hole states in ^{207}Pb [34] and previously for proton deep hole states [46].

The experimental strength distributions are compared with the available theoretical predictions of Ref. [49] for the three states and of Refs. [29,48] available only for $1g_{9/2}$ states. The microscopic QPM calculations of Vdovin [49] including $|1qh\otimes 2ph\rangle$ components describe well the strong peaking of the experimental $1g_{9/2}$ strengths.

The microscopic calculation of Bortignon and Broglia [29] predicts a somewhat smaller peaking of the $1g_{9/2}$ strength in ^{119}Sn than observed. The semimicroscopic calculations of Matveev *et al.* [48] which take into account the coupling with noncollective states via an imaginary optical potential, reproduce somewhat better the smooth distribution on the $1g_{9/2}$ peak high energy side than those of Refs. [29,49]. The QPM calculations do not reproduce the relative positions of the $1g_{9/2}$, $1f_{5/2}$, and $1f_{7/2}$ centroids, experimental data comparing better with Hartree-Fock predictions. They underestimate by nearly a factor of two the $1f_{5/2}$ and the $1f_{7/2}$ spreading widths in both isotopes and they do not explain the striking asymmetric shape of inner hole strength distributions. Similar conclusions were previously drawn for the $1g_{7/2}$ and $1g_{9/2}$ neutron inner holes in ^{207}Pb [34]. The spreading widths, but not the strength distribution asymmetric shapes, were much better described in these latter cases by Mahaux and Sartor calculations [27] in a modified mean field.

Summarizing the above comparisons, we emphasize that the present theoretical calculations do not reproduce important features of neutron inner hole responses in tin nuclei. Improved descriptions of the hole coupling with collective states, especially with high energy phonons, are needed together with renewed approaches of the coupling to the many-hole-many-particle background levels. The form factor dependence on the hole coupling to core excitations is most important in the determination of strength distributions via pick-up reactions. An improved description of this dependence taking into account the core excitation transition densities would be most interesting in this respect.

The $(\vec{d},t)$ reaction at $E_d=200$ MeV proved a quite interesting tool to study inner holes with high orbital momentum l in medium-heavy nuclei.

ACKNOWLEDGMENTS

We would like to thank P. F. Bortignon and A. Vdovin for helpful discussions and comments. We are indebted to A. Vdovin for communication of his detailed results and to A.J. Koning for communication of his multistep code and preliminary calculations. We are very grateful to Y. Bisson, G. Chesneau and R. Margaria for their efficient support before and during the experiment and to the technical staff of the Laboratoire National Saturne for its assistance. One of the authors (C.D.) was supported by a grant from the U.S. Department of Energy and the National Science Foundation.

[1] S. Galès, Ch. Stoyanov, and A. I. Vdovin, Phys. Rep. **166**, 125 (1988), and references therein.
[2] M. Sakai and K. Kubo, Nucl. Phys. **A185**, 217 (1972).
[3] M. Sekiguchi, Y. Shida, F. Soga, Y. Hirao, and M. Sakai, Nucl. Phys. **A278**, 231 (1977).
[4] T. Ishimatsa, M. Niwano, N. Kawamura, H. Ohmura, and T. Awara, Nucl. Phys. **A336**, 205 (1980).
[5] M. Matoba, H. Ejiri, H. Kametani, T. Sakae, I. Kumabe, M. Hyakutake, N. Koori, T. Maki, Phys. Lett. **149B**, 50 (1984).
[6] G. M. Crawley, J. Kasagi, S. Galès, E. Gerlic, D. Friesel, and A. Bacher, Phys. Rev. C **23**, 1818 (1981).
[7] J. Kasagi, G. M. Crawley, E. Kashy, J. Duffy, S. Galès, E. Gerlic, and D. Friesel, Phys. Rev. C **28**, 1065 (1983).
[8] M. Matoba, H. Ejiri, H. Kametani, I. Kumabe, M. Hyakutake, N. Koori, T. Sakae, and T. Maki, Nucl. Phys. **A456**, 235 (1986).
[9] S. Y. van der Werf, B. R. Kooistra, W. H. A. Hesselink, F. Iachello, L. W. Put, and R. H. Siemssen, Phys. Rev. Lett. **33**, 712 (1974).
[10] G. Berrier-Ronsin, G. Duhamel, E. Gerlic, J. Kalifa, H. Langevin-Joliot, G. Rotbard, M. Vergnes, J. Vernotte, and K. K. Seth, Phys. Lett. **67B**, 16 (1977).
[11] S. Y. van der Werf, N. M. Harakeh, L. W. Put, O. Scholten, and R. H. Siemssen, Nucl. Phys. **A289**, 141 (1977).
[12] G. Perrin, G. Duhamel, C. Perrin, E. Gerlic, S. Galès, and V. Comparat, Nucl. Phys. **A356**, 61 (1981).
[13] S. Galès *et al.*, Nucl. Phys. **A381**, 40 (1982).
[14] R. H. Siemssen, W. P. Jones, W. W. Jacobs, C. C. Foster, D. W. Miller, M. Saber, and F. Soga, Phys. Lett. **103B**, 323 (1981).
[15] R. H. Siemssen, C. C. Foster, W. W. Jacobs, W. P. Jones, D. W. Miller, M. Saber, and F. Soga, Nucl. Phys. **A405**, 205 (1983).
[16] M. Sakai, M. Sekiguchi, F. Soga, Y. Hirao, K. Yaki, and Y. Aoki, Phys. Lett. **51B**, 51 (1974).
[17] E. Gerlic, J. Kallne, H. Langevin-Joliot, J. Van de Wiele, and G. Duhamel, Phys. Lett. **57B**, 338 (1975).
[18] M. Tanaka, T. Yamagata, K. Iwamoto, S. Kishimoto, B. Saeki, K. Yuasa, T. Fukuda, I. Miura, K. Okada, M. Inoue, and H. Ogata, Phys. Lett. **78B**, 221 (1978).
[19] E. Gerlic, G. Berrier-Ronsin, G. Duhamel, S. Gales, E. Hourani, H. Langevin-Joliot, M. Vergnes, and J. Van de Wiele, Phys. Rev. C **21**, 124 (1980).
[20] H. Langevin-Joliot, E. Gerlic, J. Guillot, M. Sakai, J. Van de Wiele, A. Devaux, P. Force, and G. Landaud, Phys. Lett. **114B**, 103 (1982).
[21] H. Sakai, R. K. Bhowmik, S. Brandenburg, J. H. Van Dijk, A. G. Drentje, M. N. Harakeh, Y. Iwasaki, R. H. Siemssen, S. Y. van der Werf, and A. van der Woude, Nucl. Phys. **A441**, 640 (1985).
[22] F. Azaiez, S. Fortier, S. Gales, E. Hourani, J. M. Maison, J. Kumpulainen, and J. P. Schapira, Nucl. Phys. **A444**, 373 (1985).
[23] P. O. Söderman, A. Ringbom, J. Blomgren, N. Olsson, L. Nilsson, J. A. Bordewijk, S. Brandenburg, G. van 't Hof, M. A. Hofstee, H. van der Ploeg, S. Y. van der Werf, A. Krasznahorkay, A. Balanda, D. Chmielewska, and H. Laurent, Nucl. Phys. **A683**, 79 (2001).
[24] V. G. Soloviev, Part. Nuclei **3**, 770 (1971).
[25] V. G. Soloviev, Ch. Stoyanov, and A. I. Vdovin, Nucl. Phys. **A343**, 261 (1980), and references therein.
[26] G. F. Bertsch, P. F. Bortignon, R. A. Broglia, Rev. Mod. Phys. **55**, 287 (1983), and references therein.
[27] C. Mahaux and R. Sartor, Adv. Nucl. Phys. **20**, 1 (1991).
[28] T. Koeling and F. Iachello, Nucl. Phys. **A295**, 45 (1978).
[29] P. F. Bortignon and R. A. Broglia, Nucl. Phys. **A371**, 405 (1981).
[30] A. Vdovin and V. G. Soloviev, Part. Nuclei **14**, 237 (1983).
[31] A. Vdovin, Nguyen Dinh Thao, V. G. Soloviev, and Ch. Stoyanov, Yad. Fiz. **37**, 43 (1983); Part. Nuclei **14**, 237 (1983).
[32] J. Van de Wiele, H. Langevin-Joliot, F. Jourdan, J. Guillot, E. Gerlic, L. H. Rosier, A. Willis, C. Djalali, M. Morlet, E. Tomasi-Gustafsson, N. Blasi, S. Micheletti, and S. Y. van der Werf, Phys. Rev. C **50**, 2935 (1994).
[33] J. Van de Wiele, A. Vdovin, and H. Langevin-Joliot, Nucl. Phys. **A605**, 173 (1996).
[34] H. Langevin-Joliot, J. Van de Wiele, F. Jourdan, J. Guillot, E. Gerlic, L. H. Rosier, A. Willis, C. Djalali, M. Morlet, E. Tomasi-Gustafsson, N. Blasi, S. Micheletti, and S. Y. van der Werf, Phys. Rev. C **58**, 2192 (1998).
[35] A. J. Koning and J. M. Akkermans, Phys. Rev. C **47**, 724 (1993).
[36] J. Arvieux, S. D. Baker, A. Boudard, J. Cameron, T. Hasegawa, D. Hutcheon, C. Kerboul, G. Gaillard, and Nguyen Van Sen, Nucl. Instrum. Methods Phys. Res. A **273**, 48 (1988).
[37] B. Bonin, A. Boudard, H. Fanet, R. W. Fergerson, M. Garçon, C. Giorgetti, J. Habault, J. Le Meur, R. M. Lombard, J. C. Lugol, B. Mayer, J. P. Mouly, E. Tomasi-Gustafsson, J. C. Duchazeaubeneix, J. Yonnet, M. Morlet, J. Van de Wiele, A. Willis, G. Greeniaus, G. Gaillard, P. Markowitz, C. F. Perdrisat, R. Abegg, and D. A. Hutcheon, Nucl. Instrum. Methods Phys. Res. A **288**, 379 (1990).
[38] H. Quechon, Thesis, Orsay, 1980; J. Radin, H. Quechon, G. M. Raisbeck, and F. Yiou, Phys. Rev. C **26**, 2565 (1982).

[39] M. Beiner, H. Flocard, and Nguyen Van Giai, Nucl. Phys. **A238**, 29 (1975).
[40] Computer code DWUCK5, P. D. Kunz, University of Colorado, Boulder, CO 80309.
[41] J. Blachot, G. Marguier, Nucl. Data Sheets **73**, 81 (1994).
[42] A. van der Woude, Prog. Part. Nucl. Phys. **18**, 217 (1987).
[43] H. Feshbach, A. Kerman, and S. Koonin, Ann. Phys. (Leipzig) **125**, 429 (1980).
[44] H. Langevin-Joliot, A. J. Koning, J. Van de Wiele and J. Guillot, IPNO-DR 00-29, 2000.
[45] J. Blachot, Nucl. Data Sheets **86**, 151 (1999).
[46] J. W. A. den Herder, H. P. Blok, E. Jans, P. K. Keizer, L. Lapikas, E. N. Quint, G. van der Steenhoven, and P. K. A. de Witt Huberts, Nucl. Phys. **A490**, 507 (1988).
[47] S. P. Klevanski and R. H. Lemmer, Phys. Rev. C **28**, 1783 (1983).
[48] B. B. Matveev, B. A. Tulupov, S. E. Muraviev, and M. G. Urin, Phys. Lett. **167B**, 255 (1986).
[49] A. Vdovin (private communication).
[50] P. Doll, Nucl. Phys. **A292**, 165 (1977).
[51] J. Van de Wiele (private communication).